RSC Advances

PAPER

View Article Online
View Journal | View Issue



Cite this: *RSC Adv.*, 2026, **16**, 27223

# *In situ* formed amorphous carbon-coated $LiMn_2O_4$ cathode with long-term stability for lithium-ion batteries

Wangqiong Xu, *[a] Xianrong Li,[a] Xueqing Kang,[c] Lijuan Chen,[a] Baiyan Guo,[a] Qiling Li,*[b] Kun Xu,[a] Yiming Cao,[a] Zhe Li[a] and Yongsheng Liu*[c]

Spinel $LiMn_2O_4$ is one of the most promising cathode materials due to its green, low-cost, and abundant resources. However, issues such as manganese dissolution, electrolyte decomposition, and inadequate cycling stability have hampered its further application. Herein, we designed a modification strategy for $LiMn_2O_4$ cathodes using *N*-methyl-2-pyrrolidone (NMP), water, and ethanol mixed solution as the carbon source to *in situ* coat $LiMn_2O_4$ truncated octahedra particles. It is found that the amorphous carbon layer serves as a structure stabilization agent to enhance the electrochemical performance of $LiMn_2O_4$. Specifically, the coating carbon layer can effectively minimize the acid corrosion, facilitate $Li^+$ diffusion, improve the interface between the electrode and electrolyte, and strengthen cycle stability. As a result of these improvements, the optimized 2 mL C/$LiMn_2O_4$ sample exhibits outstanding long-term performance, with an initial discharge specific capacity of 107.6 mAh $g^{-1}$ and a capacity retention of 50.56% after 2000 cycles at 10C. This outstanding performance makes our material a promising candidate cathode for lithium-ion battery in future applications.

Received 8th April 2026
Accepted 12th May 2026

DOI: 10.1039/d6ra02942f

rsc.li/rsc-advances



## 1. Introduction

The concept of low-carbon development has fueled a dramatic increase in lithium-ion battery (LIB) production to meet the demands of energy storage.[1–6] Yet, cathode materials are pivotal in determining the overall lithium-ion battery performance.[7,8] Among various cathode materials, the spinel $LiMn_2O_4$, which exhibits natural abundance, environmental friendliness, low cost, excellent thermal stability, high operating voltage, and three-dimensional Li-ion diffusion channels, is regarded as one of the most promising candidate LIB cathode materials.[9,10] Nevertheless, the widespread use of spinel $LiMn_2O_4$ has been hindered by the dissolution loss of Mn and decomposition of the electrolyte.[11,12] Consequently, it is crucially important to develop strategies to inhibit Mn dissolution and electrolyte decomposition while enhancing surface structure stability of $LiMn_2O_4$.

Surface coating is regarded as one of the most effective strategies to alleviate Mn dissolution and electrolyte decomposition. So far, various materials have been employed to coat $LiMn_2O_4$ cathodes, such as transition metal oxides,[13–15] fluoride,[16,17] phosphate,[18,19] and carbon materials.[20,21] However, these non-carbon coating materials have poor electronic conductivity, which can limit the electronic transfer to affect the rate performance of $LiMn_2O_4$. Consequently, carbon materials with high electronic and ionic conductivity have received much attention.[22–26] The carbon coating improves the structural stability of $LiMn_2O_4$, which mainly brings the following two aspects. On the one hand, carbon coating can provide a continuous electron pathway, thus promoting fast charge transfer, which results in improved rate capability of $LiMn_2O_4$.[27] On the other hand, the carbon coating layer can avoid direct contact between the $LiMn_2O_4$ cathode and electrolyte, and protects the $LiMn_2O_4$ from the electrochemical erosion, thereby reducing the dissolution loss of Mn and decomposition of the electrolyte to enhance the cycling stability of $LiMn_2O_4$.[28] However, organic compounds (such as glucose and sucrose) as the carbon source to coat $LiMn_2O_4$; the thermal decomposition temperature of organic compounds requires *ca.* 600 °C and an $Ar/H_2$ atmosphere, which is a challenge to achieve large-scale industrial manufacturing. For example, Lee *et al.* synthesized carbon-coated $LiMn_2O_4$ nanoparticle clusters using sucrose as the carbon source and fired at 600 °C for 10 min.[29] Sun *et al.* prepared carbon-coated $LiMn_{0.85}Fe_{0.15}PO_4$ cathode material using sucrose as a carbon source and calcined for 15 h at 700 °C in a furnace purged with an $Ar/H_2$ (96/4 by vol%) mixture.[30] Therefore, it is urgent to develop a simpler method and low-cost

[a]*College of Physics and Electronic Engineering, Qujing Normal University, Qujing, Yunnan 655011, China. E-mail: xuwangqiong@mail.qjnu.edu.cn*

[b]*Yunnan Key Laboratory of Crystalline Porous Organic Functional Materials, College of Chemistry and Environmental Science, Qujing Normal University, Qujing, Yunnan 655011, China. E-mail: 839634719@qq.com*

[c]*Department of Physics, Shanghai University of Electric Power, Shanghai 200090, China. E-mail: ysliu@shiep.edu.cn*

carbon sources to prepare carbon coating on the $LiMn_2O_4$ surface.

Herein, truncated octahedra $LiMn_2O_4$ were coated by an amorphous carbon layer using *N*-methyl-2-pyrrolidone (NMP), water, and ethanol mixed solution as the carbon source. The pyrolysis of this carbon source only requires 400 °C and an air atmosphere. To the best of our knowledge, this unique strategy is rarely reported for $LiMn_2O_4$. The designed the optimized 2 mL C/$LiMn_2O_4$ cathode material demonstrates outstanding rate capability and capacity retention. This work provides a new horizon for $LiMn_2O_4$ cathode material application.

# 2 Experimental section

## 2.1 Material synthesis

The pristine $LiMn_2O_4$ sample was synthesized *via* a facile calcination process. Initially, $Mn_3O_4$ and $LiOH \cdot H_2O$ were purchased from Aladdin Reagent Co. Ltd, China and were mixed in a specific stoichiometric ratio in an agate mortar, with a 5% excess of lithium. The mixture was then heated at 500 °C for 3 h in air in the muffle furnace. The gained black sample was pulverized by hand-grounding using an agate mortar and heated at 750 °C in air for 6 h again. After cooling to room temperature, the final $LiMn_2O_4$ product was obtained. To prepare a carbon-coated $LiMn_2O_4$ sample. Firstly, 1 g of $LiMn_2O_4$ was transferred to the 50 mL beaker and then added to 15 mL of water and ethanol mixed solution ($V_{water} : V_{ethanol} = 3 : 1$). Afterward, the mixture was vigorously stirred for 5 min. Subsequently, 0.5, 2, and 4 mL of *N*-methyl-2-pyrrolidone (NMP) were dissolved in sequence in the above mixture. Next, the suspension was vigorously stirred for 2 h. This solution was then dried in an oven at 105 °C. After drying, the obtained gel was calcined at 400 °C for 1 h under an air atmosphere to obtain the carbon-coated $LiMn_2O_4$ product. The resulting powders were denoted as 0.5 mL C/$LiMn_2O_4$, 2 mL C/$LiMn_2O_4$, 4 mL C/$LiMn_2O_4$ with different NMP levels.

## 2.2 Material characterization

The crystal structure of pristine $LiMn_2O_4$ and carbon-coated $LiMn_2O_4$ was analyzed using X-ray diffraction (XRD, Ultima-IV, Rigaku, Tokyo, Japan) with the $2\theta$ range of 10–80° and scanning rate of 3° $min^{-1}$. The Rietveld refinement based on XRD data was calculated by Fullprof software. Surface morphology and element composition of the materials were investigated by scanning electron microscopy (SEM, Gemini 450, ZEISS, Jena, Germany) with an accelerating voltage of 5.0 kV and transmission electron microscopy (TEM, JEM-2100F, JEOL, Japan) equipped with an energy-dispersive X-ray detector at an accelerating voltage of 200 kV, respectively. The Image J program was used to calculate the average grain sizes of the materials. The surface chemical information and Mn valence state were analyzed by X-ray photoelectron spectroscopy (XPS, Thermo Fischer, ESCALAB 250Xi, USA) using the monochromatic Al-$K_\alpha$ as the excitation source and C 1s (284.8 eV) for a reference binding energy. The microstructure and atomic-scale information of the samples were analyzed using spherical aberration-corrected transmission electron microscopy (JEM Grand ARM300F, JEOL, Japan). The electrodes of $LiMn_2O_4$ and 2 mL C/$LiMn_2O_4$ after 2000 cycles used for XRD and XPS characterizations were disassembled from coin cells.

## 2.3 Electrochemical tests

The electrochemical performances of the prepared pristine $LiMn_2O_4$ and carbon-coated $LiMn_2O_4$ were evaluated by using a CR2025-type coin cell, where pristine $LiMn_2O_4$ and carbon-coated $LiMn_2O_4$ electrodes were fabricated by mixing of active materials, carbon black, and polyvinylidene fluoride (PVDF) in a weight ratio of 8 : 1 : 1 dissolved in *N*-methyl-2-pyrolidone (NMP) solvent to form a slurry in air using a high-energy Micro-Vibration Mill. The slurry was then evenly spread onto an Al foil current collector using a coating blade and dried in a vacuum oven at 120 °C for 12 h to remove residual solvents. The vacuum-dried foils were cut into 14 mm diameter discs using a punching machine to serve as the working electrode. The mass loadings of the active materials per the working electrode sheet area ranged from 1.3 to 2.0 mg $cm^{-2}$. The CR2025-type coin cells were assembled in an argon-filled glove box ($O_2$ < 0.01 ppm, $H_2O$ < 0.01 ppm). The lithium metal sheet (thickness of 0.45 cm) was used as the negative electrode. And the Celgard 2400 polypropylene membrane was used as the separator. The 1 mol $L^{-1}$ $LiPF_6$ in a mixture of ethylene carbonate (EC) and dimethyl carbonate (DMC) (1 : 1 in volume) was used as the electrolyte. Galvanostatic charge–discharge tests were conducted using a computer-controlled LAND-CT2001 battery testing system. All electrochemical tests were conducted at room temperature. The cycling voltage window was set at a range of 3.0–4.5 V. Cycling test was carried out at 10C (1C = 148 mAh $g^{-1}$) for 2000 cycles. The rate capability test was performed at rates of 0.5C, 1C, 2C, 3C, 5C, and 10C. Cyclic voltammetry (CV) and electrochemical impedance spectroscopy (EIS) measurements were performed on the coin cell configuration using a CHI604E electrochemical workstation (Shanghai Chenhua, China). The CV measurements were conducted at scan rates of 0.05, 0.1, 0.15, 0.2, and 0.25 mV $s^{-1}$ within a voltage range of 3.6–4.5 V (*vs.* $Li/Li^+$). The EIS tests were carried out with 10 mV perturbation amplitude in the frequency range of $10^{-1}$ to $10^5$ Hz in automatic sweep mode.

# 3 Results and discussion

## 3.1 Structural and surface analysis

X-ray diffraction analysis is used to investigate the effect of different NMP contents on the crystal structure of $LiMn_2O_4$. As shown in Fig. 1a, the diffraction patterns of four samples are well indexed to the standard spinel $LiMn_2O_4$ (JCPDS 35-0782), confirming that the introduction of NMP would not induce any crystal structure alteration of $LiMn_2O_4$. Also, no diffraction peaks of carbon were observed, which may be attributed to the carbon layer is inherently amorphous and the contents is low. To better analyze the sample structure, the lattice parameters of $LiMn_2O_4$ and carbon-coated $LiMn_2O_4$ are calculated through XRD Rietveld refinement, as shown in Fig. 1c–f. Each fitted

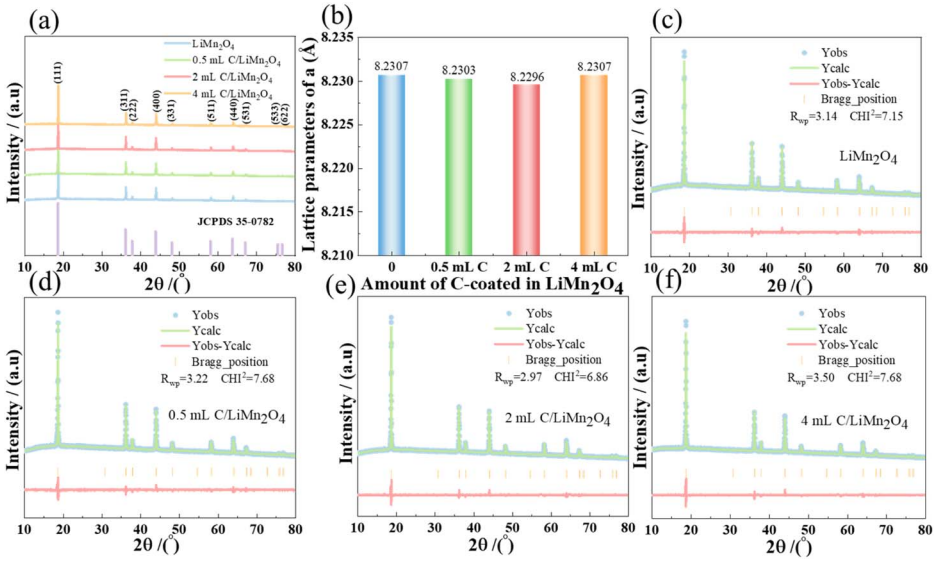


Fig. 1 (a) XRD patterns of $LiMn_2O_4$ and carbon-coated $LiMn_2O_4$ with different NMP contents; (b) lattice parameters *vs.* amount of carbon coated plot; (c–f) XRD Rietveld refinement results of $LiMn_2O_4$ and carbon-coated $LiMn_2O_4$ with different NMP contents.

curve is well indexed to the measured data ($R_{wp}$ < 10, $CHI^2$ < 10),[31,32] indicating refinement results are reliable. Fig. 1b presents the relationship between lattice parameters and the amount of carbon coating. It can be seen that the lattice parameters of the four samples are basically the same. Therefore, it can be further verified that the carbon coating does not cause structural changes of $LiMn_2O_4$ bulk phase.

The morphology of $LiMn_2O_4$ and carbon-coated $LiMn_2O_4$ with different NMP contents was characterized using scanning electron microscopy. As shown in Fig. 2a–d, both materials exhibited similar truncated octahedra morphologies. Histograms of particle size distribution of $LiMn_2O_4$ and carbon-coated $LiMn_2O_4$ are examined on the basis of micrograph analysis (Fig. S1). The average particle size of $LiMn_2O_4$ and the carbon-coated $LiMn_2O_4$ sample is similar (*ca.* 129.27 nm), which indicates the carbon coating does not influence the morphology and particle size of $LiMn_2O_4$. To verify the existence of the carbon coating layer, EDS elemental mapping has been performed (Fig. 2e). Fig. 2e exhibits Mn and O elements are homogeneously distributed in the central region of the particle, while the C element is highly concentrated in the outer region and shows a high intensity. This provides strong evidence that the carbon layer is coated on the surface of $LiMn_2O_4$.

In order to further confirm that carbon is coated on the surface of $LiMn_2O_4$, high-resolution C 1s XPS spectra are measured as shown in the Fig. 3a. The C 1s spectra of 2 mL C/$LiMn_2O_4$ (Fig. 3a) exhibit three deconvoluted peaks comprising of C–C, C–O, and C=O located at 284.82, 286.52, and 288.47 eV, respectively,[24,33] which guarantees the carbon coating. Notably, the Mn valence state of $LiMn_2O_4$ and 2 mL C/$LiMn_2O_4$ were investigated (Fig. 3b). The Mn 2p spectral peaks were separated into the Mn $2p_{3/2}$, Mn $2p_{1/2}$, and satellite peak due to spin–orbit splitting,[34,35] which displays the mixing of $Mn^{3+}$ and $Mn^{4+}$. It is worth noting that the binding energy of Mn $2p_{3/2}$ is similar for

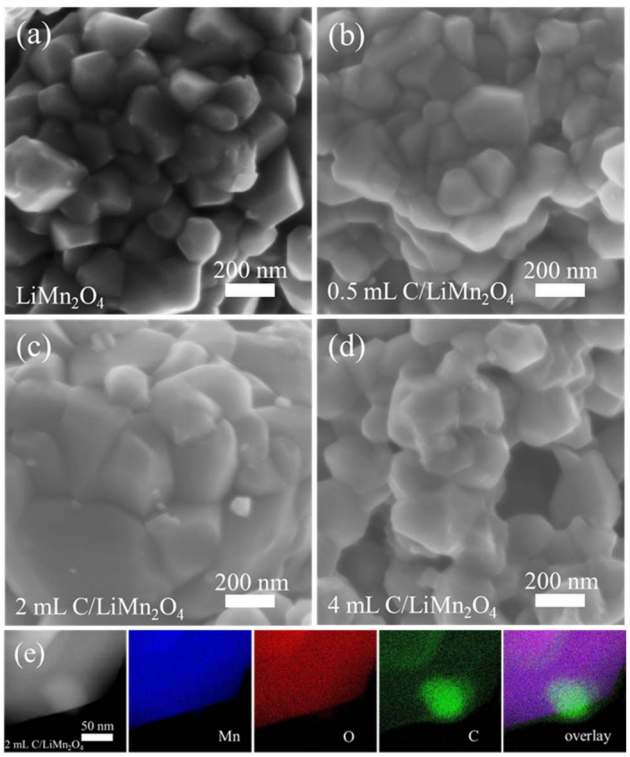


Fig. 2 (a–d) SEM images of $LiMn_2O_4$ and carbon-coated $LiMn_2O_4$ with different NMP contents; (e) STEM images and corresponding EDS elemental maps of 2 mL C/$LiMn_2O_4$.

$LiMn_2O_4$ and 2 mL C/$LiMn_2O_4$, which suggests the carbon coating had less effect on the Mn valence state. The detailed Mn valence state information was obtained, which fitted the Mn $2p_{3/2}$ spectra using the CasaXPS software; the results were shown in Fig. 3c, d and Tables S1, S2. It was found that the

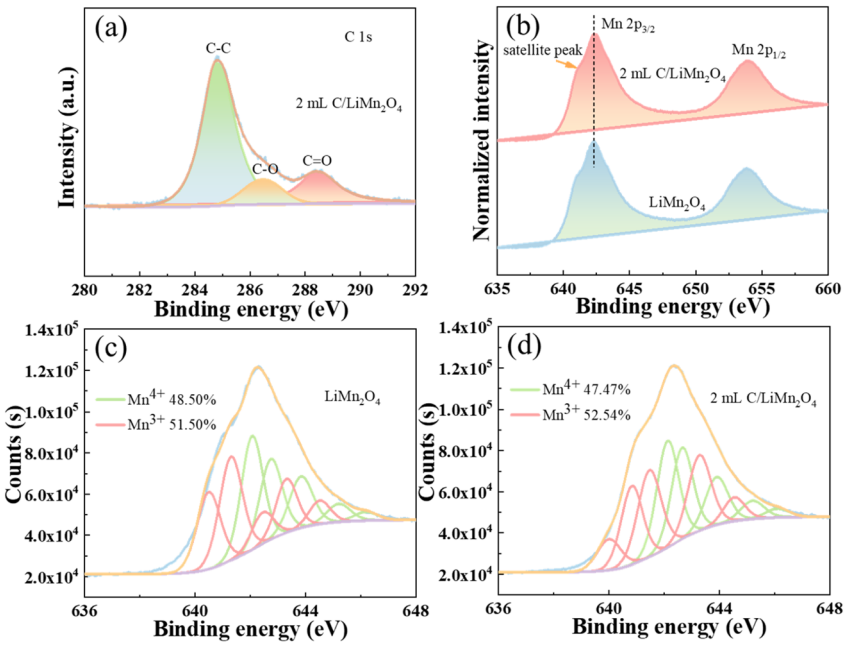


Fig. 3 (a) High-resolution C 1s XPS spectra of 2 mL C/$LiMn_2O_4$; (b) high-resolution Mn 2p XPS spectra of $LiMn_2O_4$ and 2 mL C/$LiMn_2O_4$; fitted spectra of Mn $2p_{3/2}$ for (c) $LiMn_2O_4$ and (d) 2 mL C/$LiMn_2O_4$.

concentrations of $Mn^{3+}$ and $Mn^{4+}$ in the $LiMn_2O_4$ sample were 51.50% and 48.50%, respectively, whereas those in the 2 mL C/$LiMn_2O_4$ sample were 52.54% and 47.47%, respectively. This further suggests that carbon coating does not cause Mn valence state changes of $LiMn_2O_4$.

### 3.2 Analysis of the atomic-level structural

To better confirm the carbon coating on the surface of $LiMn_2O_4$, high-angle annular dark-field scanning transmission electron microscopy (HAADF-STEM) of $LiMn_2O_4$ and 2 mL C/$LiMn_2O_4$ was conducted, as shown in Fig. 4. Fig. 4a and c displays the overall morphology of the probed particle for $LiMn_2O_4$ and 2 mL C/$LiMn_2O_4$, respectively. It can be seen that the carbon layer is coated on the surface of the $LiMn_2O_4$ particle (Fig. 4c). The coating thickness of the carbon layer is about 9.53 nm (Fig. 4d). Detailed crystalline structures between the bulk and the surface of the $LiMn_2O_4$ and 2 mL C/$LiMn_2O_4$ were disclosed by the high-resolution HAADF images (Fig. 4b and e). It was found that the bulk and surface structure of $LiMn_2O_4$ remains the same Mn diamond configuration from the magnified images in Fig. 4b, with the brighter and weaker dots corresponding to Mn1 and Mn2 columns, respectively. Moreover, Fig. 4f and g confirm that the intensity of Mn1 columns is twice that of Mn2 columns due to different stacking density.[36] However, no observable contrast in Li and O sites in Fig. 4b. This is because the HAADF image is only sensitive to heavy elements.[37,38] For the carbon-coated $LiMn_2O_4$ samples, the bulk region possesses the same Mn diamond configuration (Fig. 4e and h). However, the surface region illustrates that the coated carbon layer is amorphous. The carbon layer coated on the surface of $LiMn_2O_4$, which facilitates the electron conduction and prevents HF from the electrolyte to etch $LiMn_2O_4$ cathode.

### 3.3 Electrochemical testing

In order to evaluate the effectiveness of carbon coating on the spinel $LiMn_2O_4$ material performance, electrochemical tests were conducted and are shown in Fig. 5. Fig. 5a shows the long-term cycling performance of $LiMn_2O_4$ and carbon-coated $LiMn_2O_4$ with different NMP contents between 3.0 and 4.5 V at 10C at 25 °C. It can be observed that the initial discharge specific capacities of $LiMn_2O_4$, 0.5 mL C/$LiMn_2O_4$, 2 mL C/$LiMn_2O_4$, and 4 mL C/$LiMn_2O_4$ are 57.7, 91.7, 107.6, and 82.9 mAh $g^{-1}$, respectively, with corresponding capacity retention rates after 2000 cycles of 39.34%, 44.60%, 50.56%, and 46.56% (Fig. 5a and b). As the coating amount increases, the initial discharge specific capacity and capacity retention rates initially increase and then reduce. This trend can be attributed to the carbon coating layer, which enhances charge transfer between particles, where an optimal carbon coating amount enhances the battery performance. Apart from that, the coulombic efficiency retains over 99% from the 2nd cycle (Fig. 5a), suggesting the excellent reversibility of the electrochemical reaction for 2 mL C/$LiMn_2O_4$. These results imply that 2 mL C/$LiMn_2O_4$ has optimal long-term performance among the modified materials.

Fig. 5c presents the rate capability curves of the $LiMn_2O_4$ and carbon-coated $LiMn_2O_4$ with different NMP contents. As can be seen in Fig. 5c, the discharge specific capacities of $LiMn_2O_4$, 0.5 mL C/$LiMn_2O_4$, 2 mL C/$LiMn_2O_4$, and 4 mL C/$LiMn_2O_4$ decrease with increasing rates, whereas the 2 mL C/$LiMn_2O_4$ exhibits superior performance compared to the other three samples at various rates. The improved high-rate performance

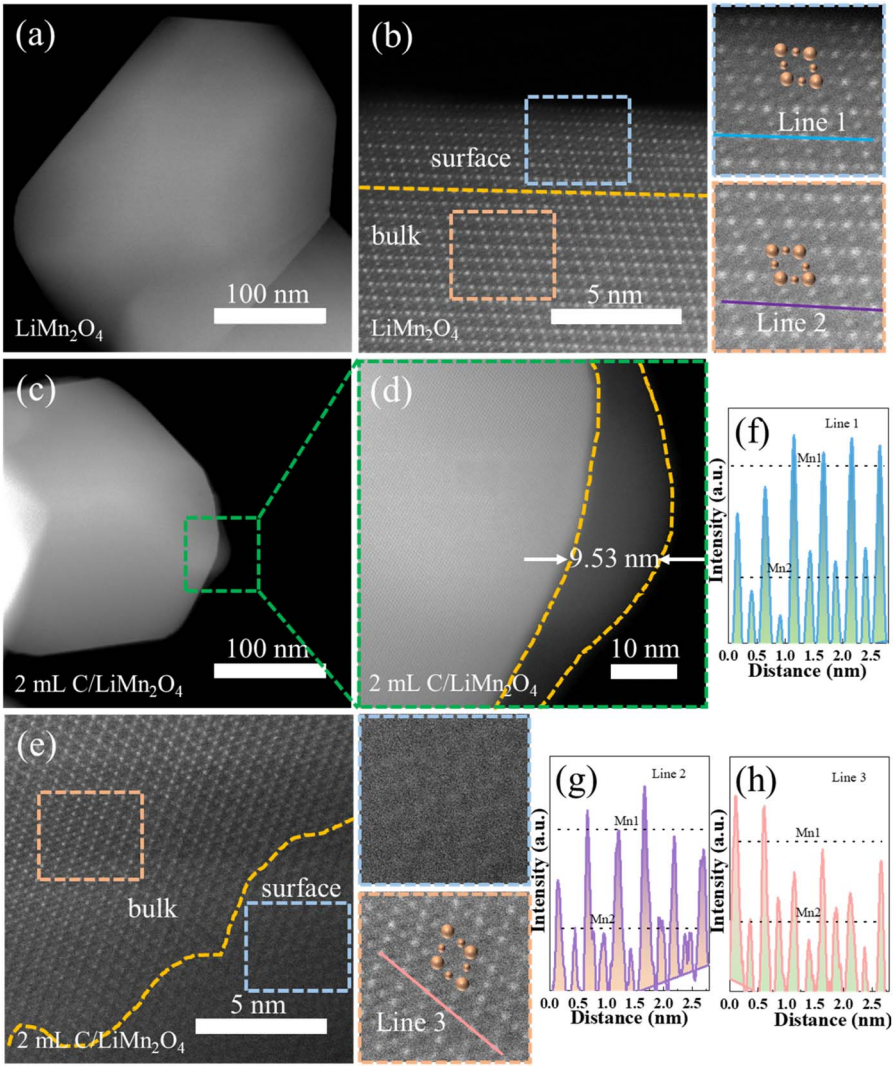


Fig. 4 (a) The low-magnification STEM image and (b) atomic-resolution HAADF image of the $LiMn_2O_4$ cathode; (c) the low-magnification and (d) medium-magnification STEM image of 2 mL C/$LiMn_2O_4$ cathode, (e) atomic-resolution HAADF image of 2 mL C/$LiMn_2O_4$ cathode; The right exhibits surface and bulk region magnified images in the HAADF image from the blue and orange frames, respectively. The surface and the bulk area are demarcated by the golden dotted line. Mn atoms are labeled in orange. (f–h) Line profile corresponding to the blue and purple lines in the magnified image of $LiMn_2O_4$, and the pink line in the magnified image of 2 mL C/$LiMn_2O_4$.

of 2 mL C/$LiMn_2O_4$ can be attributed to the carbon coating layer, which protects the active material from undesirable chemical reactions. Additionally, it is worth noting that all initial charge–discharge of the four samples at low C rate presented two pairs of distinct plateaus platforms (Fig. 5d–g), corresponding to Li-ions extracted/inserted from/into spinel $LiMn_2O_4$.[39] Moreover, the initial charge/discharge special capacity of 2 mL C/$LiMn_2O_4$ shows slower decay at various C-rates, suggesting that an appropriate carbon coating layer can inhibit the electrolyte decomposition on the electrode surfaces. However, the plateau platforms of the initial charge–discharge of the four samples aren't obvious at 10C high rates (Fig. 5h), which can be attributed to the increase in electrochemical polarization at high current density.

To further explore the mechanism of $Li^+$ diffusion during the charge–discharge process, cyclic voltammetry (CV) analyses were performed on $LiMn_2O_4$ and 2 mL C/$LiMn_2O_4$, as shown in Fig. 6a, b and S2a–c. It can be seen that both CV profiles reveal the doublet redox peaks at around 4.0 and 4.15 V, corresponding to the deintercalation and intercalation of $Li^+$, respectively.[40] The peak positions agree with the plateaus in the charge–discharge curves (Fig. 5d and f). Additionally, before cycling and after 2000 cycles at 10C, 2 mL C/$LiMn_2O_4$ exhibits higher peak currents, suggesting that carbon coating enhances the lithium storage capacity of $LiMn_2O_4$. However, after 2000 cycles at 10C, the peak areas of the CV curve of $LiMn_2O_4$ and 2 mL C/$LiMn_2O_4$ decrease, which indicates that the capacity reduces significantly. With the growth of the scan rate for CV curves (Fig. S2a and b), the redox peaks become broader and the peak current increases, which results from the irreversible processes in $Li^+$ insertion/extraction in/from the spinel structure. However, the carbon coating $LiMn_2O_4$ has lower electrochemical polarization

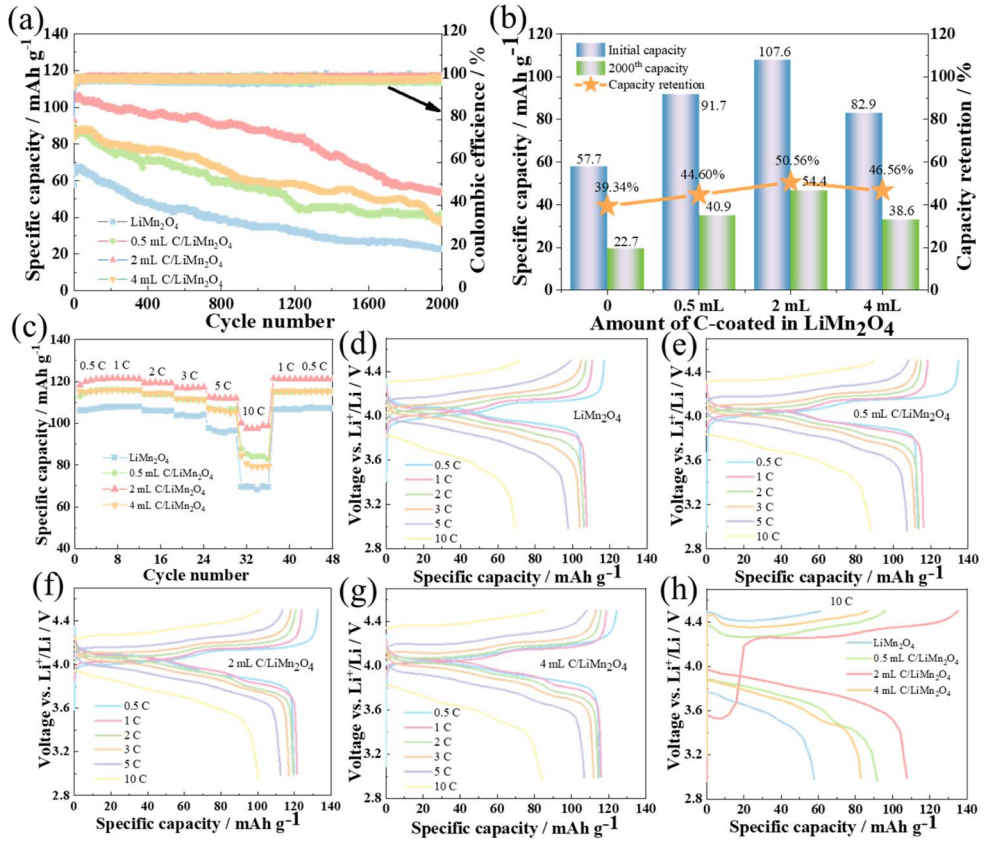


Fig. 5 Electrochemical performance of $LiMn_2O_4$ and carbon-coated $LiMn_2O_4$ with different NMP contents: (a) long-term cycling performance at 10C for 2000 cycles at 25 °C; (b) comparison of the difference value of initial capacity, 2000th capacity, and capacity retention rates at 10C for 2000 cycles at 25 °C, respectively; (c) rate capability at various C rates from 0.5C to 10C; (d–g) the charge–discharge curves at different current rates; (h) initial charge–discharge curves at 10C.

than that of $LiMn_2O_4$. Specifically, the relationship of the reduction peak current at bare $LiMn_2O_4$ and 2 mL C/$LiMn_2O_4$ with the square root of scan rate is studied (Fig. S2c). Corresponding to lithium-ion diffusion coefficients ($D_{Li^+}$) of $LiMn_2O_4$ and 2 mL C/$LiMn_2O_4$ were calculated, the detailed information is shown in the supporting information. The lithium-ion diffusion coefficient of 2 mL C/$LiMn_2O_4$ was calculated as $5.72 \times 10^{-15}$ $cm^2$ $s^{-1}$, which is significantly higher than that of $LiMn_2O_4$ ($1.26 \times 10^{-15}$ $cm^2$ $s^{-1}$), indicating that carbon coating facilitates the diffusion of $Li^+$.

To further analyze the effect of carbon coating on the diffusion kinetics of $Li^+$, the EIS measurement of $LiMn_2O_4$ and 2 mL C/$LiMn_2O_4$ before and after 2000 cycles at a 10C rate was conducted. The Nyquist plots of $LiMn_2O_4$ and 2 mL C/$LiMn_2O_4$ before and after 2000 cycles and the equivalent circuit used for fitting the Nyquist plots are shown in Fig. 6c and S2d. Fig. 6c and S2d show EIS plots that consist of high-frequency and medium-region semicircles, and an oblique straight line at low frequency region.[41] The inset of Fig. 6c and S2d shows the equivalent circuits comprising resistors ($R$) at the high frequency and medium region, constant phase elements (CPE), and a Warburg element ($W$) at the low frequency region.[29] The semicircle in the high-frequency region represents the impedance of the electrolyte between the two electrodes ($R_1$). The semicircle in the medium frequency region corresponds to the charge transfer impedance ($R_2$), and the oblique straight line at low frequency region indicates the Warburg impedance associated with the diffusion of $Li^+$ ions. To obtain specific impedance values, the fitting of the EIS curve by an equivalent circuit was performed and is listed in Table S3. It can be seen that the charge transfer impedance ($R_2$) values of 2 mL C/$LiMn_2O_4$ before and after cycling are significantly lower than those of $LiMn_2O_4$. This can be attributed to the fact that carbon coating has excellent electron transport, which facilitates $Li^+$ transport by improving surface diffusion kinetics.[22] To quantitatively evaluate the $Li^+$ diffusion coefficient ($D_{Li^+}$), linear fitting of $Z'$ *vs.* $\omega^{-1/2}$ for $LiMn_2O_4$ and 2 mL C/$LiMn_2O_4$ before cycling is presented in Fig. 6d, the corresponding calculated process is shown in the SI. As shown in Fig. 6d, the Warburg coefficient ($\sigma$) of $LiMn_2O_4$ and 2 mL C/$LiMn_2O_4$ is 129.27 and 119.87 $\Omega$ $s^{-1/2}$, respectively. Therefore, $Li^+$ diffusion coefficient ($D_{Li^+}$) of 2 mL C/$LiMn_2O_4$ was calculated as $2.74 \times 10^{-15}$ $cm^2$ $s^{-1}$, which is higher than that of $LiMn_2O_4$ ($2.36 \times 10^{-15}$ $cm^2$ $s^{-1}$), indicating that carbon coating facilitates the diffusion rate of $Li^+$.

### 3.4 Analysis of cycled cathodes

To assess the crystal stability of carbon-coated $LiMn_2O_4$, XRD analysis was performed on the pure $LiMn_2O_4$ and 2 mL C/

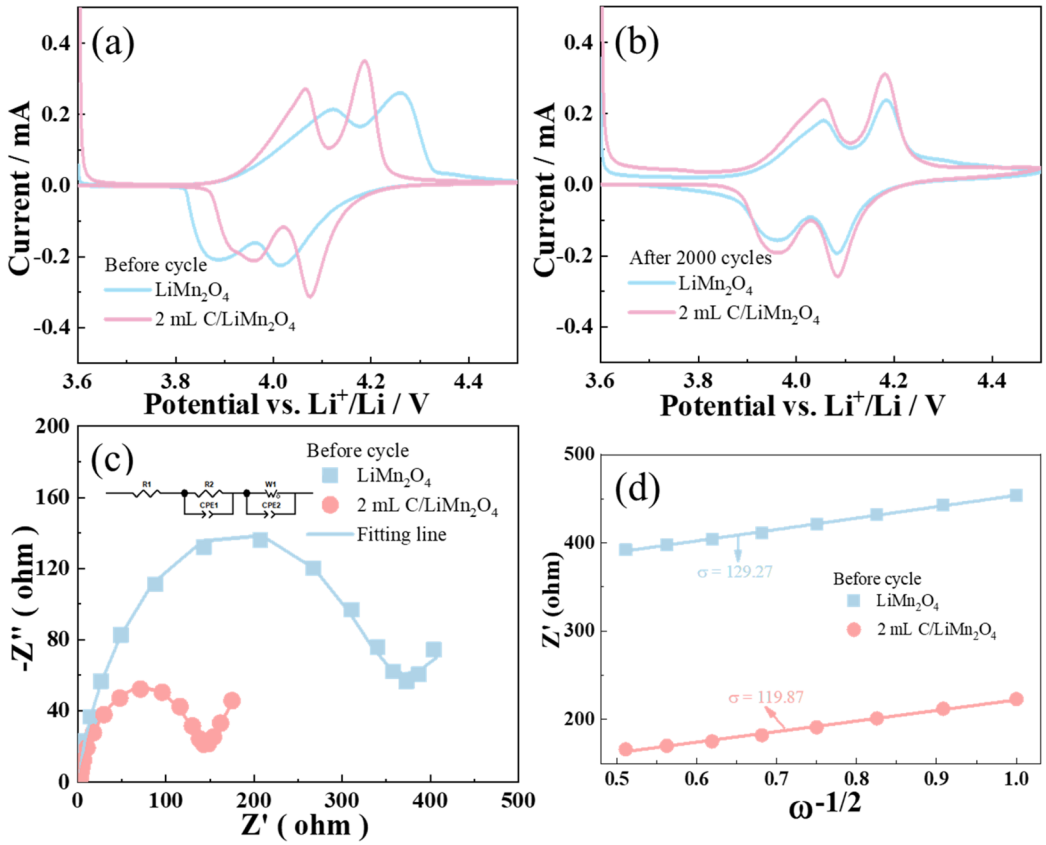


Fig. 6 CV curves of the bare $LiMn_2O_4$ and 2 mL C/$LiMn_2O_4$ (a) before cycling and (b) after 2000 cycles with scan rates of 0.05 mV $s^{-1}$; (c) EIS plots of bare $LiMn_2O_4$ and 2 mL C/$LiMn_2O_4$ before cycling and the inset shows the equivalent circuits; (d) linear fitting of $Z'$ *vs.* $\omega^{-1/2}$.

$LiMn_2O_4$ before and after cycling. As shown in Fig. 7a and b, it can be seen that the diffraction peaks of pure $LiMn_2O_4$ and 2 mL C/$LiMn_2O_4$ after cycling remain similar to those before cycling, apart from the appearance of the C impurity peaks derived from the conductive agent carbon black and Al impurity peaks derived from the Al foil current collector, suggesting that the spinel-type $LiMn_2O_4$ structure is still maintained. However, it can be clearly observed from Fig. 7a that after 2000 cycles, the intensity of the (111) diffraction peak of pure $LiMn_2O_4$ is weaker than that before the cycle, indicating that the crystallinity of pure $LiMn_2O_4$ is decreased. The (111) diffraction peak of 2 mL C/$LiMn_2O_4$ after 2000 cycles still has high intensity (Fig. 7b), indicating that 2 mL C/$LiMn_2O_4$ has high cyclic stability. This result indicates that carbon coating can suppress Mn dissolution and alleviate side reactions at the electrode surface, thereby improving the structural stability of $LiMn_2O_4$.

To gain a deeper understanding of the stability of 2 mL C/$LiMn_2O_4$, XPS tests were also carried out after cycling. In the C

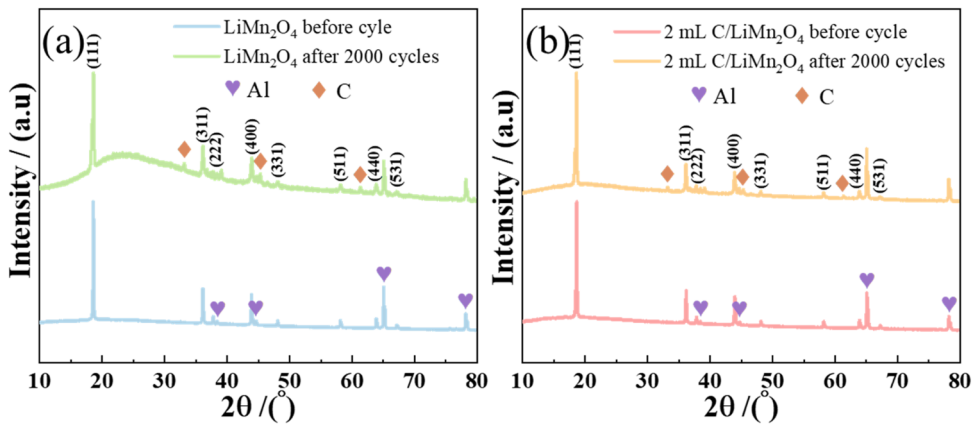


Fig. 7 Comparison of XRD patterns before cycling and after 2000 cycles at 10C of (a) $LiMn_2O_4$ and (b) 2 mL C/$LiMn_2O_4$.

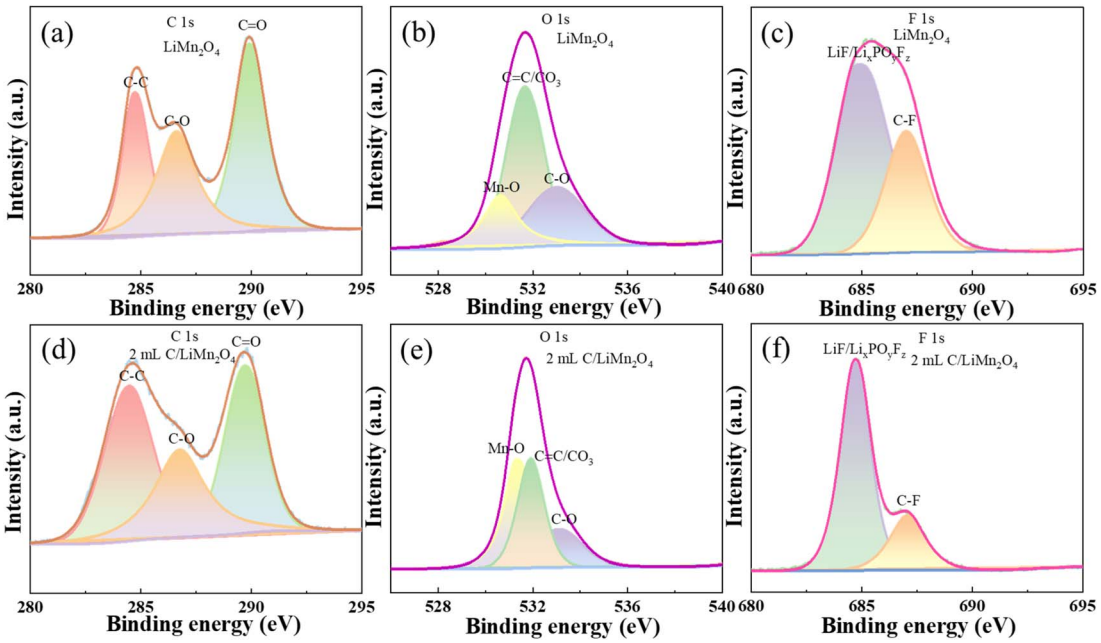


Fig. 8 XPS spectra of C 1s, O 1s, and F 1s for (a–c) $LiMn_2O_4$ and (d–f) 2 mL C/$LiMn_2O_4$ after 2000 cycles at 10C.

1s spectra of $LiMn_2O_4$ and 2 mL C/$LiMn_2O_4$ after 2000 cycles at 10C (Fig. 8a, d), the C–C peak originates from conductive carbon black and carbon coating, the C–O and C=O peaks are derived from the decomposition products of the organic electrolyte and carbon coating.[42] It can be seen that the intensity of the C–C peak for 2 mL C/$LiMn_2O_4$ is higher than that of $LiMn_2O_4$. However, the intensity of the C–O and C=O peaks for 2 mL C/$LiMn_2O_4$ is lower than that of $LiMn_2O_4$, indicating that carbon is still coated on the surface of $LiMn_2O_4$ after 2000 cycles at 10C and can inhibit the decomposition of the electrolyte. In the O 1 s spectra, 2 mL C/$LiMn_2O_4$ exhibits stronger Mn–O peaks (Fig. 8b and e), suggesting that carbon coating can prevent the release of oxygen from the electrode surface. Comparing F 1s spectra, it can be discovered that the weaker peaks of LiF/$Li_xPO_yF_z$ and C–F on the 2 mL C/$LiMn_2O_4$ surface were detected (Fig. 8c and f), further verifying that carbon coating can suppress the decomposition of $LiPF_6$. Therefore, carbon coating can inhibit the decomposition of the electrolyte and prevent oxygen release from the material surface, thus enhancing the interfacial stability and long-term cycling performance of $LiMn_2O_4$.

## 4 Conclusions

In summary, an amorphous carbon layer coating on the surface of the $LiMn_2O_4$ cathode material is synthesized through a facile calcination process. It was found that the introduction of the carbon layer didn't change the bulk structure, surface morphology, and Mn oxidation state of the $LiMn_2O_4$. However, the carbon layer serves as a structure stabilization agent to reduce Mn dissolution, improve the interface between the electrode and electrolyte, and inhibit electrolyte decomposition, which enhances $Li^+$ migration. The optimized 2 mL C/$LiMn_2O_4$ sample exhibits the most excellent long-term performance with the initial discharge specific capacity of 107.6 mAh $g^{-1}$ and the capacity retention of 50.56% after 2000 cycles at 10C, which is much higher than that of $LiMn_2O_4$ (57.7 mAh $g^{-1}$, 39.34%). This work provides a simple and efficient modification strategy for developing high-performance $LiMn_2O_4$ cathode materials.

## Author contributions

Wangqiong Xu: writing – review & editing, writing –original draft, funding acquisition. Xianrong Li: data curation. Xueqing Kang: data curation. Lijuan Chen: formal analysis. Baiyan Guo: software. Qiling Li: visualization, validation, conceptualization, investigation. Kun Xu: resources. Yiming Cao: resources. Zhe Li: resources. Yongsheng Liu: supervision, resources, methodology.

## Conflicts of interest

The authors declare no competing financial interest.

## Data availability

All relevant data are included in the paper. The data supporting this study's findings are available from the corresponding author upon reasonable request.

Supplementary information (SI) is available. See DOI: https://doi.org/10.1039/d6ra02942f.

## Acknowledgements

This work was supported by the Fundamental Research Project of Yunnan Province (202301AT070239), the Special Basic Cooperative Research Programs of Yunnan Provincial

Undergraduate Universities' Association (grant No. 202401BA070001-129), the Special Basic Cooperative Research Innovation Programs of Qujing Science and Technology Bureau & Qujing Normal University (KJLH2023ZD02).

## Notes and references

1 J. E. Zhou, Y. L. Li, M. Y. Zou, X. Hu, X. S. Miao, X. X. Xie, X. M. Lin, J. Qian, C. Yang and R. J. Chen, *Adv. Funct. Mater.*, 2025, **35**, 2501603.
2 X. C. Ye, X. Y. Fei, M. J. Liu, H. Gao, B. L. Qiu, H. Y. Yin, Z. H. Zhang and L. Y. S. Lee, *Adv. Mater.*, 2025, **37**, 2416537.
3 Y. Y. Bi, S. L. Tian, Y. Zhang, A. K. Huang, P. Kumar, Z. Ma, W. Q. Liu and J. Ming, *ACS Energy Lett.*, 2026, **11**, 1670–1679.
4 J. Guo, J. Y. Du, W. Q. Liu, G. Huang and X. B. Zhang, *Angew. Chem., Int. Ed.*, 2024, **63**, e202406465.
5 Y. Zhang, Z. Y. Hu, Y. Y. Bi, S. L. Tian, H. R. Sun, K. Li, W. Q. Liu, L. S. Sun, W. Liu and D. Wang, *ACS Sustainable Chem. Eng.*, 2025, **13**, 5381–5393.
6 Y. F. Cui, Z. B. Zhuang, Z. L. Xie, R. F. Cao, Q. Hao, N. Zhang, W. Q. Liu, Y. H. Zhu and G. Huang, *ACS Nano*, 2022, **16**, 20730–20738.
7 H. J. Yang, L. Yan, J. M. Qin, Y. Wang, N. Hu and T. Zhou, *Adv. Funct. Mater.*, 2026, **36**, e15317.
8 J. Guo, H. B. Chen, D. P. Wang, W. Q. Liu, G. Huang and X. B. Zhang, *Sci. Bull.*, 2024, **69**, 3237–3246.
9 W. H. Zeng, F. J. Xia, J. Wang, J. L. Yang, H. Y. Peng, W. Shu, Q. Li, H. Wang, G. Wang, S. C. Mu and J. S. Wu, *Nat. Commun.*, 2024, **15**, 7371.
10 J. Z. Du, Z. W. Sun, B. H. Peng, X. M. Xu, L. J. Fu, Y. H. Chen, L. L. Liu, X. Liu and Y. P. Wu, *Adv. Funct. Mater.*, 2025, **35**, 2421179.
11 S. Q. Zhong, Y. C. Huang, F. C. Zhang, H. Z. Wang, P. W. Liu, J. W. Liu, Z. Q. Li, Y. Z. Li and Z. G. Lu, *Adv. Funct. Mater.*, 2025, **35**, 2414602.
12 G. C. Tan, S. Wan, J. J. Chen, H. Q. Yu and Y. Yu, *Adv. Mater.*, 2024, **36**, 2310657.
13 R. X. Yin, W. H. Xu and Z. W. Zhao, *Desalination*, 2026, 620.
14 Q. L. Li, W. Q. Xu, H. L. Bai, J. M. Guo and C. W. Su, *Ionics*, 2016, **22**, 1343–1351.
15 Y. F. He, H. Pham, X. H. Liang and J. Park, *J. Power Sources*, 2023, **586**, 233682.
16 T. Wang, W. Wang, D. Zhu, X. B. Duan, Z. Q. Wet and Y. G. Chen, Chin, *J. Inorg. Chem.*, 2014, **30**, 2461–2468.
17 Y. P. Wang, X. Y. Wang, S. Y. Yang, H. B. Shu, Q. L. Wei, Q. Wu, Y. S. Bai and B. N. Hu, *J. Solid State Electrochem.*, 2012, **16**, 2913–2920.
18 S. Zhao, Y. Bai, L. H. Ding, B. Wang and W. F. Zhang, *Solid State Ionics*, 2013, **247**, 22–29.
19 C. B. Qing, Y. Bai, J. M. Yang and W. F. Zhang, *Electrochim. Acta*, 2011, **56**, 6612–6618.
20 M. J. Lee, E. Lho, P. Bai, S. Chae, J. Li and J. Cho, *Nano Lett.*, 2017, **17**, 3744–3751.
21 D. Yao, Z. D. Wu, J. J. Song, L. Cai, Y. Ouyang, W. Lei, S. Mathur, F. Q. Wu and Q. L. Hao, *ACS Appl. Energy Mater.*, 2020, **3**, 4840–4851.
22 J. F. Wang, W. Liu, S. Liu, J. X. Chen, H. L. Wang and S. P. Zhao, *Electrochim. Acta*, 2016, **188**, 645–652.
23 G. Chen, B. Y. Peng, R. Han, N. X. Chen, Z. Z. Wang and Q. Wang, *Ceram. Int.*, 2020, **46**, 20985–20992.
24 V. Selvamani, N. Phattharasupakun, J. Wutthiprom and M. Sawangphruk, *Sustainable Energy Fuels*, 2019, **3**, 1988–1994.
25 M. Molenda, R. Dziembaj, E. Podstawka, L. M. Proniewicz and Z. Piwowarska, *J. Power Sources*, 2007, **174**, 613–618.
26 K. Peng and T. F. Peng, *Ceram. Int.*, 2014, **40**, 15345–15349.
27 X. L. Yu, J. J. Deng, X. Yang, J. Li, Z. H. Huang, B. H. Li and F. Y. Kang, *Nano Energy*, 2020, **67**, 104256.
28 J. Y. He, Y. Ren, S. X. Zhuang, S. Y. Jiang, X. X. Pan, G. X. Sun, B. Zhu, Y. F. Wen and X. D. Li, *Chem. Commun.*, 2023, **59**, 13050–13053.
29 S. Lee, Y. Cho, H. K. Song, K. T. Lee and J. Cho, *Angew. Chem., Int. Ed.*, 2012, **51**, 8748–8752.
30 Y. K. Sun, S. M. Oh, H. K. Park and B. Scrosati, *Adv. Mater.*, 2011, **23**, 5050–5054.
31 Y. K. Pan, Y. H. Li, L. Hu, Y. D. Yang, J. C. Guo and S. J. Yang, *J. Power Sources*, 2025, **650**, 237527.
32 P. A. Ferreirs and G. H. Rubiolo, *J. Mater. Sci.*, 2018, **53**, 2802–2811.
33 C. Tomon, S. Sarawutanukul, N. Phattharasupakun, S. Duangdangchote, P. Chomkhuntod, N. Joraleechanchai, P. Bunyanidhi and M. Sawangphruk, *Commun. Chem.*, 2022, **5**, 54.
34 H. Q. Li, N. Chen, S. J. Zhang, Y. H. Han, X. Gao, H. Q. Chen, Y. X. Bai and W. S. Gao, *ACS Appl. Mater. Interfaces*, 2025, **17**, 21269–21280.
35 E. Kim, J. Lee, J. Park, H. Kim and K. W. Nam, *Nano Lett.*, 2025, **25**, 619–627.
36 W. Q. Xu, C. Z. Song, R. J. Qi, Y. H. Zheng, Y. N. Wu, Y. Cheng, H. Peng, H. C. Lin and R. Huang, *ACS Appl. Mater. Interfaces*, 2022, **14**, 55528–55537.
37 S. Y. Yang, P. Yan, W. D. Bao, H. Y. Zhu, X. C. Cai, L. Q. Zhao, Y. Zhang, W. Y. Lin, Y. D. Deng, Y. F. Wu and J. Xie, *ACS Energy Lett.*, 2023, **8**, 4278–4286.
38 R. P. Qing, J. L. Shi, D. D. Xiao, X. D. Zhang, Y. X. Yin, Y. B. Zhai, L. Gu and Y. G. Guo, *Adv. Energy Mater.*, 2016, **6**, 1501914.
39 K. Chudzik, M. Lis, M. Swietoslawski, M. Bakierska, M. Gajewska and M. Molenda, *J. Power Sources*, 2019, **434**, 226725.
40 S. J. Jiang, S. Wang, Y. J. Li, S. P. Hao, X. M. Xi, S. W. Liu, Y. K. Xiong, J. C. Zheng and P. P. Zhang, *Mater. Today Energy*, 2022, **29**, 101096.
41 G. J. Yan, P. Y. Li, S. Xie, J. J. Li, W. J. Li, J. C. Zheng and M. L. Yuan, *Ceram. Int.*, 2025, **51**, 12029–12034.
42 S. Wang, S. J. Jiang, Y. J. Li, Z. L. Tan, S. P. Hao, J. C. Yang and Z. J. He, *J. Power Sources*, 2023, **579**, 233292.